

$U(1)$ symmetry-enriched toric code

Kai-Hsin Wu,^{1,*} Alexey Khudorozhkov,¹ Guilherme Delfino,¹ Dmitry Green,^{2,1} and Claudio Chamon¹

¹*Department of Physics, Boston University, 590 Commonwealth Avenue, Boston, Massachusetts 02215, USA*

²*AppliedTQC.com, ResearchPULSE LLC, New York, NY 10065, USA*

(Dated: May 19, 2023)

We propose and study a generalization of Kitaev’s \mathbb{Z}_2 toric code on a square lattice with an additional global $U(1)$ symmetry. Using Quantum Monte Carlo simulation, we find strong evidence for a topologically ordered ground state manifold with indications of UV/IR mixing, i.e., the topological degeneracy of the ground state depends on the microscopic details of the lattice. Specifically, the ground state degeneracy depends on the lattice tilt relative to the directions of the torus cycles. In particular, we observe that while the usual compactification along the vertical/horizontal lines of the square lattice shows a two-fold ground state degeneracy, compactifying the lattice at 45° leads to a three-fold degeneracy. In addition to its unusual topological properties, this system also exhibits Hilbert space fragmentation. Finally, we propose a candidate experimental realization of the model in an array of superconducting quantum wires.

I. INTRODUCTION

Topological phases of matter have been, increasingly, drawing attention from physics and quantum information communities over the past several decades [1]. These special quantum phases exhibit exotic properties such as their topological ground state degeneracy (TGSD) and the excitation content that cannot be captured by conventional Ginzburg-Landau theory.

A gapped quantum system is considered to possess (*intrinsic*) *topological order* if it has degenerate ground states that are locally indistinguishable. The TGSD is robust against any local perturbation and depends only on the topology of the underlying spatial manifold [1–5]. Topologically ordered phases exhibit long-range entanglement and support local excitations with fractional exchange statistics (anyons) that cannot be created in isolation by a local process [6–10]. Topological order in two spatial dimensions has been extensively studied in various different realizations such as: quantum spin liquids [8, 11–21], fractional quantum Hall states [10, 22–24], superconductors [25], topological quantum field theories [26, 27], etc.

More recently, a notion of *fracton topological order* has been introduced [28–35]. Fractonic phases of matter exhibit fractionalized excitations (fractons) that cannot be created in pairs. Unlike an anyon, which is created at the end points of a string-like operator (Wilson line) and can freely move across space, a single fracton is immobile, since fractons are created at the corners of membrane- or fractal-like operators. Another difference with the usual topological order is that in fractonic systems the ground state degeneracy (GSD) depends not only on the topology of the manifold, but also on the microscopic properties of the model, such as the system size and the lattice geometry. This is a manifestation of UV/IR mixing in quantum field theory [36, 37].

Additional classification of topological phases of matter arise from an interplay between symmetry and topological order. Even in the absence of intrinsic topological order, a system invariant under a symmetry can exhibit several distinct phases that cannot be adiabatically connected to each other, unless one violates the symmetry or closes the energy gap. These phases do not break the considered symmetry and are known as *symmetry-protected topological* (SPT) phases, with notable examples including free-fermionic topological insulators in 2D [38–40] and 3D [41–44], topological superconductors [45], as well as interacting bosonic SPTs [46–49]. Furthermore, the distinct phases protected by a symmetry need not lack intrinsic topological order. In fact, the presence of symmetry can give rise to adiabatically disconnected phases with distinct topological orders, so called *symmetry-enriched topological* (SET) phases, where anyons transform non-trivially under the symmetry [50–58].

Despite numerous attempts [19, 49, 51, 52, 54, 56–62], to-date there is no unifying theory for all topological orders. In the case of SETs, many classification attempts rely on constructing representative exactly solvable models that serve as fixed points for each phases. In addition, the majority of the work has been done on finite symmetry groups and only recently has there been an attempt to classify $U(1)$ -symmetric SETs [58].

In this work we pose the question of what happens as one tries to enrich the usual \mathbb{Z}_2 toric code with a global $U(1)$ symmetry. Although topological order has been previously enriched with $U(1)$ symmetry through the addition of extra degrees of freedom [58, 63], here we take a different approach and restrict the usual toric code Hamiltonian to only interactions that are $U(1)$ symmetric. The presence of the extra symmetry imposes additional constraints on the ground state loop dynamics, compared to the conventional \mathbb{Z}_2 toric code. We refer to the 2D lattice model as the “ $U(1)$ symmetry-enriched toric code” – or “ $U(1)$ toric code” for short. Its Hamiltonian is not a sum of commuting projectors, and hence not exactly solvable in any obvious way. However, the

* khwu@bu.edu

model does not have a sign problem, which allows us to study the model via large scale Quantum Monte Carlo (QMC) simulation.

One of the motivations to study the model is its relation to the so called WXY model [64], which consists of two-body interaction terms between “matter” and “gauge” spins, located at the vertices and edges of a square lattice, respectively. It possesses combinatorial \mathbb{Z}_2 gauge symmetry [64–68] in addition to a global $U(1)$ symmetry. The $U(1)$ toric code is believed to emerge after one integrates out the matter spins in the WXY model. However, unlike the former, the WXY model is difficult to study numerically since the unit cell is too large for exact diagonalization and the sign problem prevents us from employing Quantum Monte Carlo.

Through our numerical studies on the $U(1)$ toric code, we observe a degenerate ground state manifold where non-local quantum numbers are necessary to distinguish the states. We also observe the existence of UV/IR mixing, which manifests itself in the change of the ground state degeneracy upon contracting the lattice on a torus through different compactification vectors. A similar flavor of a UV/IR mixing was explored in Ref. [69]. It differs from the usual manifestation of UV/IR mixing in fractonic models, where the GSD typically depends only on the system size. In addition to its unusual GSD properties, the model displays Hilbert space fragmentation [70–72]. Finally, we propose a physical realization of the model in a mesh of Josephson-coupled superconducting quantum wires.

II. LATTICE MODEL

One simple way to arrive at the model of interest is to begin with Kitaev’s \mathbb{Z}_2 toric code [8] and then enrich it by an additional global $U(1)$ symmetry. (A second way, less direct but closer to experimental settings, is presented in Sec.V.) Consider a square lattice with sites $s \equiv (i, j)$, where i, j are the x - and y -coordinates, and elementary lattice vectors $\hat{x} \equiv 2\hat{e}_x = (1, 0)$, $\hat{y} = 2\hat{e}_y = (0, 1)$. A spin-1/2 degree of freedom is located on each link ℓ . We say $\ell \in s$ if the link ℓ is one of the four links adjacent to the site s , i.e., if $\ell = s \pm \hat{e}_{x,y}$. We define a star operator $A_s(\theta)$ as the product of four spin-1/2 operators $\sigma_\ell^\theta = \cos(\theta)\sigma_\ell^x + \sin(\theta)\sigma_\ell^y$ on the links adjacent to site s ,

$$A_s(\theta) = \prod_{\ell \in s} \sigma_\ell^\theta. \quad (1)$$

σ^x , σ^y , and σ^z are the usual Pauli spin operators. The generalized star operator $A_s(\theta)$ for any angle θ is invariant under a \mathbb{Z}_2 local transformation, generated by the product of σ^z operators on the links of a given plaquette p :

$$B_p = \prod_{\ell \in \partial p} \sigma_\ell^z. \quad (2)$$

In other words, $[A_s(\theta), B_p] = 0$, for all s, p and θ , which is similar to the usual toric code for fixed θ .

The global $U(1)$ symmetry can be introduced by averaging $A_s(\theta)$ over all angles:

$$\mathcal{A}_s = \frac{1}{2\pi} \int_0^{2\pi} d\theta A_s(\theta). \quad (3)$$

Keeping only the surviving terms in the integral, this star operator can be written in terms of spin raising and lowering operators as

$$\begin{aligned} \mathcal{A}_s &= \sigma_{s+\hat{e}_x}^+ \sigma_{s+\hat{e}_y}^+ \sigma_{s-\hat{e}_x}^- \sigma_{s-\hat{e}_y}^- \\ &+ \sigma_{s+\hat{e}_x}^+ \sigma_{s+\hat{e}_y}^- \sigma_{s-\hat{e}_x}^+ \sigma_{s-\hat{e}_y}^- \\ &+ \sigma_{s+\hat{e}_x}^- \sigma_{s+\hat{e}_y}^+ \sigma_{s-\hat{e}_x}^- \sigma_{s-\hat{e}_y}^+ + \text{h.c.}, \end{aligned} \quad (4)$$

with $\sigma_\ell^\pm = (\sigma_\ell^x \pm i\sigma_\ell^y)/2$. It is easy to check that the stars \mathcal{A}_s in Eq. (3) are invariant under a global z -axis rotation,

$$U_z = \exp\left(-i\frac{\alpha}{2}M_z\right), \quad (5)$$

where $M_z = \sum_\ell \sigma_\ell^z$ is the total magnetization in the z -direction. Namely

$$U_z \mathcal{A}_s U_z^\dagger = \frac{1}{2\pi} \int_0^{2\pi} d\theta A_s(\theta + \alpha) = \mathcal{A}_s. \quad (6)$$

The magnetization conservation is also apparent from Eq. (4), since, in the σ^z basis, every term flips exactly two spins up and two spins down. The Hamiltonian can now be formally written as the sum over all possible star and plaquette operators,

$$H = -\lambda_A \sum_s \mathcal{A}_s - \lambda_B \sum_p B_p. \quad (7)$$

We note that this model is not a sum of commuting projectors: neighboring stars do not commute, i.e., $[A_s, A_{s'}] \neq 0$ if s is adjacent to s' .

One can easily check that the Hamiltonian commutes with total magnetization M_z and all the plaquettes $\{B_p\}$,

$$[H, M_z] = 0 \quad \text{and} \quad [H, B_p] = 0 \quad \forall p, \quad (8)$$

which are conserved quantities associated to the global $U(1)$ and local \mathbb{Z}_2 gauge symmetry, respectively.

For any local closed loop γ composed of a sequence of connected links, the loop operator

$$W(\gamma) = \prod_{\ell \in \gamma} \sigma_\ell^z \quad (9)$$

commutes with the Hamiltonian, $[H, W(\gamma)] = 0$, and can be represented as a product of plaquette operators B_p enclosed by γ . When putting the system on a torus, two additional loop-operators, W_x and W_y , defined along the shortest non-contractible loops that wind

around the torus in the x and y directions are also conserved. The $U(1)$ toric code can be block-diagonalized in the common eigen basis of these operators, so that each sector is characterized by a set of independent conserved quantities $\{M_z, W_x, W_y, \{B_p\}\}$. We are particularly interested in the four sectors categorized by $W_x = \pm 1, W_y = \pm 1$, as they underscore the topological features. In the following, we refer to these four sectors as topological sectors, with respective quantum numbers $(W_x, W_y) = (+, +), (+, -), (-, +)$ and $(-, -)$.

Interestingly, we find that within each symmetry block the Hilbert space further splits into multiple even smaller fragments (or Krylov subsectors), indicating that the system exhibits Hilbert space fragmentation [70–72]. An exact diagonalization (ED) study that we carried out suggests that in the vicinity of zero magnetization, the Hilbert space of each symmetry sector is dominated by a single large fragment, an indication of weak Hilbert space fragmentation. This implies that in these symmetry sectors the lowest energy eigenstates belong to this large fragment (see Appendix A). We note that the fragmentation structure for a different system whose dynamics we can map to that of the $U(1)$ toric code in the sector of $\{W_x = +1, W_y = +1, \{B_p = +1\}\}$ has been shown to be weak [73–76], which is consistent with our ED results.

III. NUMERICAL RESULTS

The $U(1)$ toric code in Eq. (7) is free of a sign problem, which allows us to study it via the Stochastic Series Expansion Quantum Monte Carlo (SSE QMC) method using a generalized version of the sweeping cluster update algorithm [77–79]. This algorithm is designed to perform simulations not only within any symmetry sector, but within any Hilbert space fragment, specified by an initial basis state from that fragment (See Appendix B for technical details). In our studies we always choose an initial state within the largest fragment in the symmetry sector of interest.

In this work, we focus on the even parity sector where all $B_p = +1$, which encompasses the ground states of the Hamiltonian (7) for sufficiently large λ_B (we set $\lambda_A = 1$ henceforth). Within the even parity sector, we then study all four topological sectors that are characterized by $W_x = \pm 1$ and $W_y = \pm 1$. We are particularly interested in whether the lowest energy states from different topological sectors are degenerate, as this degeneracy might indicate the existence of topological order in the system.

In addition, we examine the dependence of the ground state properties of the lattice on a torus with various compactifications. We introduce two orthogonal compactification vectors \vec{L}_1 and \vec{L}_2 , parameterized by two non-negative integers a and b , as

$$\begin{aligned}\vec{L}_1 &= L(a\hat{x} + b\hat{y}) \\ \vec{L}_2 &= L(-b\hat{x} + a\hat{y}),\end{aligned}\quad (10)$$

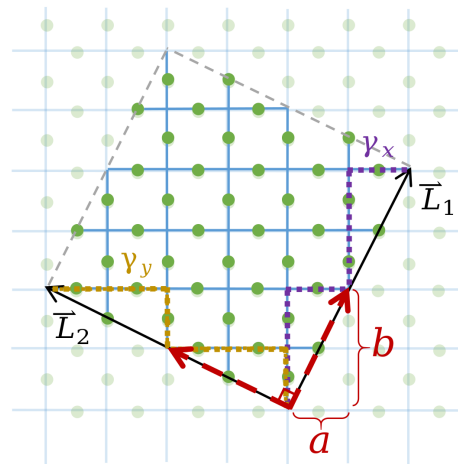


FIG. 1. An example of a lattice with compactification $a = 1, b = 2$ and linear size $L = 2$. Any vector \vec{r} is identified with vectors $\vec{r} + \vec{L}_1$ and $\vec{r} + \vec{L}_2$. The whole lattice is shown in bright colors, while the shaded region denotes repeating parts of the lattice due to the periodic boundary condition. Two non-contractible loops γ_x and γ_y shown as purple and yellow dotted lines respectively along two compactification vectors \vec{L}_1 and \vec{L}_2 .

where L (a positive integer) is the linear system size. We choose the vector (a, b) to be the shortest integer vector in its direction, i.e., a and b are coprimes. Vectors \vec{L}_1, \vec{L}_2 define the compactification scheme in the sense that any spatial vector \vec{r} is identified with vectors $\vec{r} + \vec{L}_1$ and $\vec{r} + \vec{L}_2$. An example of a small lattice with a non-trivial compactification scheme is shown in Fig. 1.

We define the non-contractible loops γ_x and γ_y along \vec{L}_1 and \vec{L}_2 directions as shown in Fig. 1 by the purple and yellow dotted lines, respectively. The non-contractible loop operators are given by the products of spin operators along these two loops as

$$W_x = \prod_{i \in \gamma_x} \sigma_i^z, \quad (11)$$

$$W_y = \prod_{i \in \gamma_y} \sigma_i^z. \quad (12)$$

Note that there is freedom in the choice of non-contractible strings entering the definition of the operators W , since two strings operators going around the torus in the same direction can be deformed into each other by multiplications of B_p operators.

Also note that even though the symmetry generators, $M_z, W_x, W_y, \{B_p\}$, are independent of each other, their quantum numbers might be incompatible. Compatibility of quantum numbers depends on the compactification scheme, as well as the linear size L . For example, in the case of $a = 1, b = 0$ compactification, it is not possible to have a zero magnetization state within the $(+, +)$ and $(-, -)$ topological sectors when the linear size L is odd (see Appendix C).

Below we explore in detail two lattice compactifications on a torus: A) 0° -tilt compactification, corresponding to $a = 1$, $b = 0$ – the usual compactification along the vertical and horizontal lines of the square lattice; and B) 45° -tilt compactification, with $a = 1$, $b = 1$. We focus on the cases with L even, for which we observe that the ground states have magnetization $M_z = 0$ in of all topological sectors. Cases with L odd are explored in Appendix E, and compactifications with other tilt angles are discussed in Appendix F.

A. 0° -tilt compactification

We observe a finite energy gap of order $\mathcal{O}(1)$ between sectors $(W_x, W_y) = (+, -)$ and $(-, -)$ for all system sizes L considered. The sectors $(+, -)$ and $(-, +)$ have identical energy spectra due to the C_4 rotation symmetry of the lattice. On the other hand, the energy difference between sectors $(+, +)$ and $(-, -)$ vanishes as L increases, with the lowest energy state in the sector $(-, -)$ in all cases (see Fig. 2). We find that this energy difference becomes essentially zero within error bars beyond system sizes as small as $L = 6$. We conclude that the system has a two-fold degeneracy associated to sectors $(+, +)$ and $(-, -)$, to which we henceforth refer as a topological degeneracy (TGSD) distinguished by quantum numbers associated to operators (W_x, W_y) defined on non-contractible loops.

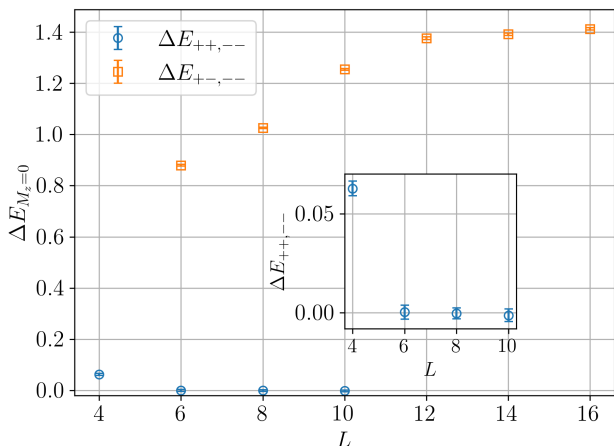


FIG. 2. Energy gaps between the ground states in different topological sectors as a function of system size L in the 0° -tilt compactification. E_{W_x, W_y, W'_x, W'_y} labels the energy difference between sectors (W_x, W_y) and (W'_x, W'_y) . For all system sizes, the sector $(-, -)$ has the lowest energy. The inset shows that the finite size gap $\Delta E_{+, -} \rightarrow 0$ as $L \rightarrow \infty$. The results indicate that the system has a two-fold TGSD.

The observation of an $\mathcal{O}(1)$ energy separation between topological sectors suggests that the system is gapped. However, this observation alone does not rule out the possibility that the system is gapless within each of the

$(+, +)$ and $(-, -)$ ground state sectors. To establish that the system is, in fact, gapped within each of these sectors, we compute the spin-spin correlation functions along the x -direction, $C(r)$, and along the 45° diagonal direction, $C_d(r)$, defined as

$$C(r) = \frac{1}{L} \sum_{\alpha} \sigma_{(\hat{e}_x + \alpha \hat{y})}^z \sigma_{(\hat{e}_x + \alpha \hat{y}) + r \hat{x}}^z, \quad (13a)$$

$$C_d(r) = \frac{1}{L} \sum_{\alpha} \sigma_{(\hat{e}_x + \alpha \hat{e}_{xy})}^z \sigma_{(\hat{e}_x + \alpha \hat{e}_{xy}) + r \hat{e}_{xy}}^z, \quad (13b)$$

where $\hat{e}_{xy} = \hat{e}_x + \hat{e}_y$, $\hat{e}_{\bar{x}y} = -\hat{e}_x + \hat{e}_y$. We observe that both correlation functions decay rapidly to zero within a short distance on the order of two lattice sites, as shown in Fig. 3(a), for the $(-, -)$ sector (see Appendix D for correlations in other topological sectors). This rapid decay is consistent with the absence of long-range magnetic order and provides evidence that the system is gapped within each topological sector.

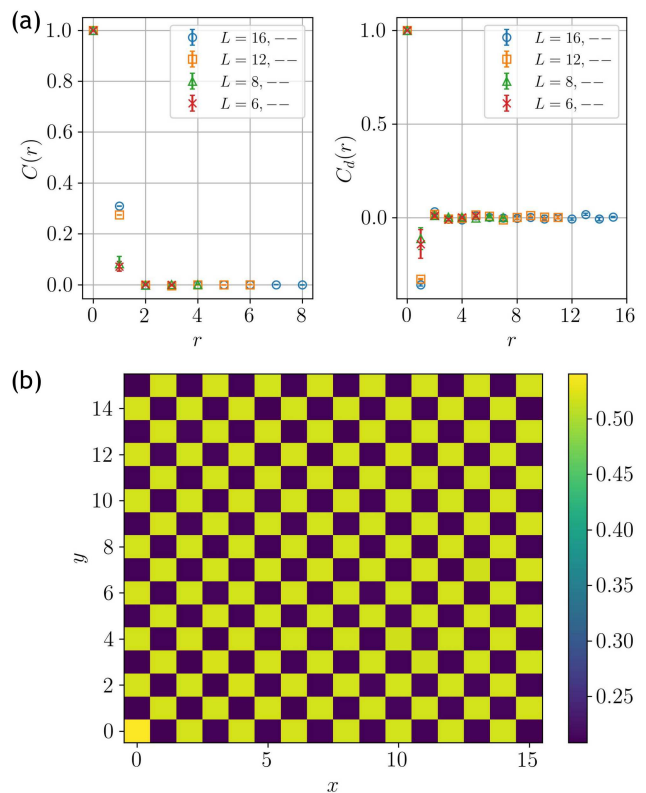


FIG. 3. (a) Spin-spin correlation function in the x - and 45° -direction ($C(r)$ and $C_d(r)$ respectively) for different system sizes, L . The correlation function decays to zero rapidly, indicating that the system is gapped. (b) Intensity plot of the star-star correlation $\langle \mathcal{A}_{s=(0,0)} \mathcal{A}_{s'=(x,y)} \rangle$, indicating translational symmetry breaking. The system size is $L = 16$. Both results shown here correspond to the 0° -tilt compactification, in the sector $(-, -)$ and with $M_z = 0$.

We observe a spatial checkerboard pattern in the measurements of the star-star correlator $\langle \mathcal{A}_s \mathcal{A}_{s'} \rangle$, shown in

Fig. 3(b). This pattern suggests that the ground states spontaneously break translation symmetry. This staggered pattern appears in both degenerate topological sectors $(-, -)$ and $(+, +)$, indicating the coexistence of spontaneous symmetry breaking with topological degeneracy, i.e., the total ground state degeneracy is 4, the product of the two-fold TGSD by a factor of 2 originating from the symmetry breaking.

B. 45°-tilt compactification

We repeat the studies above for the 45°-tilted lattice. The essential observation here is that the state in the $(-, -)$ sector has higher energy than the states in the other three sectors $(+, +)$, $(+, -)$, and $(-, +)$, which are degenerate, thus yielding a three-fold TGSD (see Fig. 4). We find, again, that the spin-spin correlation functions are fast decaying for all three states in the ground state manifold, just as in the case of 0°-tilt compactification. This suggests the absence of long range magnetic order and provides strong evidence for a gapped ground state manifold (see Appendix. D).

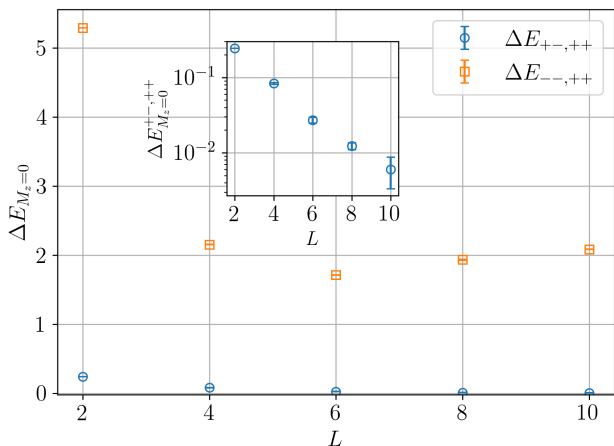


FIG. 4. Energy gaps between the ground states in different topological sectors as a function of system size in the 45°-tilt compactification. The notation is common to that of Fig. 2. The state in the $(-, -)$ sector has higher energy, and is separated from the states in the other three sectors $(+, +)$, $(+, -)$, and $(-, +)$, which are degenerate. [Note that $(+, -)$ and $(-, +)$ sectors have identical energy spectra due to the C_4 rotation symmetry of the lattice.]

IV. DISCUSSION OF THE GROUND STATE DEGENERACY

The results above establish numerically that the TGSD depends on the tilt angle of the compactification of the lattice. For the 0°-tilt, we find a TGSD of two (sectors $(+, +)$ and $(-, -)$), while for the 45°-tilt we find a

TGSD of three (sectors $(+, +)$, $(+, -)$, and $(-, +)$). This result is peculiar for two reasons. First, a change of the TGSD upon changing the compactification of the lattice is a clear manifestation of UV/IR mixing, a feature quite common in gapped fractonic phases. In fractonic systems the TGSD typically depends on the system size and on the relative dimensions of the lattice [28–34], while here it depends on the choice of compactification directions (vectors) defining a torus.

Second, the three-fold topological degeneracy in the 45°-tilt poses a puzzle. The $U(1)$ toric code Hamiltonian Eq. (7) is time-reversal symmetric. The observed three-fold topological degeneracy is quite unusual when coming from a time-reversal (T) invariant \mathbb{Z}_2 gauge theory. Typically, topological quantum field theories with T -symmetry are characterized by Hilbert space dimensions that are either the square of an integer or numbers that decompose into Pythagorean prime ones [80]. Neither is consistent with a degeneracy of three. One logical possibility is that the T -symmetry is spontaneously broken. If this is the case, it is not manifest through long-range magnetic order, since we find that the ground states have zero magnetization and that the spin-spin correlation functions decay exponentially.

Since we do not have an analytical solution with which to compare the numerical features that we observe, we follow a phenomenological approach to see what features the theory must have in order to be consistent with our numerical results. Let us posit the existence of non-local tunneling operators $T_{x,y}$, which are not necessarily unitary, that flip the eigenvalues of the non-local winding loop operators $W_{x,y}$. As opposed to the usual toric code, one cannot explicitly write down these operators (or at least we do not know of a way, yet).

Consider first the case of 45°-tilt compactification, and operators $T_x^{45^\circ}$ and $T_y^{45^\circ}$, depicted as a red solid-arrow and a black dashed-arrow in Fig. 5; these operators change the eigenvalues of W_x and W_y , respectively. The three ground states can be indexed as

$$|++\rangle, |-\rangle \sim T_x^{45^\circ} |++\rangle, |+-\rangle \sim T_y^{45^\circ} |++\rangle. \quad (14)$$

To be consistent with the numerical result, that the fourth state $|--\rangle$, is an excited state and not yet another ground state, the application of the product $T_x^{45^\circ} T_y^{45^\circ}$ to the reference state $|++\rangle$ must be orthogonal to the ground state manifold, or equivalently, i.e., it must annihilate the reference state in the ground state manifold,

$$T_x^{45^\circ} T_y^{45^\circ} |++\rangle \sim 0. \quad (15)$$

This scenario parallels that of $SU(2)_2$ topological order (hosting Ising anyons), where one can insert fluxes (corresponding to the tunneling operators, $T_x^{45^\circ}$ or $T_y^{45^\circ}$) through one or the other hole of the torus and switch ground states, but not insert flux through both (see, for example, Ref. [81]). The net effect is to make the fourth ground state inaccessible as in Eq. (15). (Refs. [82, 83] give examples of systems with $SU(2)_2$ topological order

where the tunneling operators $T_{x,y}$ can be constructed and their algebra is studied.)

These tunneling operators also allow us to propose an heuristic argument that connects the topological ground state degeneracy in the two compactification schemes. For the case of 0° -tilt compactification, the two tunneling operators $T_x^{45^\circ}$ and $T_y^{45^\circ}$ (again depicted as a red solid-arrow and a black dashed-arrow in Fig. 5) wind across the torus along the $+45^\circ$ and -45° directions. Along both directions, the tunneling operators flip both winding loop eigenvalues W_x and W_y , and we write the two ground states as

$$|++\rangle, |--\rangle \sim T_x^{45^\circ} |++\rangle \sim T_y^{45^\circ} |++\rangle. \quad (16)$$

Because both $T_x^{45^\circ}$ and $T_y^{45^\circ}$ have the same action on $|++\rangle$, they provide us with only one additional state, $|--\rangle$, and thus a topological ground state degeneracy of two in the 0° -tilt compactification.

Again, the argument for the exclusion of the fourth sector, $|--\rangle$, from the ground state manifold in the case of 45° -tilt compactification parallels that in the case of Ising anyons. These arguments suggest a logical possibility that the $U(1)$ toric code may realize non-Abelian topological order. A thorough investigation of this possibility is left for future work.

One way to test the robustness of the ground state degeneracy is to perturb the Hamiltonian (7) using arbitrary local terms, such as longitudinal and transverse magnetic fields

$$H \rightarrow \tilde{H} = H - g_x \sum_{\ell} \sigma_{\ell}^x - g_z \sum_{\ell} \sigma_{\ell}^z. \quad (17)$$

However, we encounter the following difficulties in numerically carrying out such tests using both ED or QMC. ED is limited to small system sizes, posing the numerical challenge of distinguishing effects due to the perturbation from those due to the finite size (the correlation length, even if small as suggested by the decay of spin-spin correlations in Fig. 3, is not zero). In the case of QMC, our update algorithm is build so as to conserve all quantum numbers, $\{B_p\}$, M_z , W_x , W_y , and cannot incorporate perturbations that break the conservation of these quantities without significant modification of the update scheme. (It is unclear what modifications would be required in the QMC update algorithm to accommodate such perturbations.)

V. A PHYSICAL REALIZATION OF THE STAR-TERM OF THE $U(1)$ TORIC CODE

Here we illustrate how the four-spin interaction term \mathcal{A}_s in our Hamiltonian in Eq. (4) appears naturally in a physical set-up proposed in Ref. [64] using arrays of superconducting quantum wires coupled via Josephson junctions. Consider, for each star s , a 4×4 array of vertical and horizontal wires intersecting at 16 crossings,

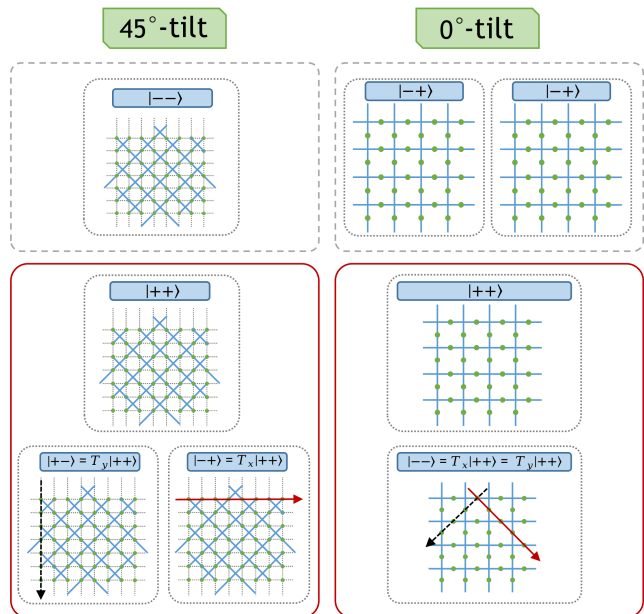


FIG. 5. Mapping between topological sectors in 0° -tilt (right side) and 45° -tilt (left side) compactifications. The ground state manifold is depicted with the red frames, while topological sectors with excited lowest energy states are depicted with gray dashed frames. We assume existence of non-local and non-unitary tunneling operators, $T_x^{45^\circ}$ (red arrows) and $T_y^{45^\circ}$ (dashed black arrows), that in the 45° -tilt case take the state $|++\rangle$ to states $|--\rangle$ and $|+-\rangle$, respectively. Simultaneous application of both tunneling operators to $|++\rangle$ annihilates the state, and therefore $|--\rangle$ does not belong to the ground state manifold. In the 0° -tilt case, assuming the same orientation of the tunneling operators with respect to the microscopic details of the lattice, both $T_x^{45^\circ}$ and $T_y^{45^\circ}$ take state $|++\rangle$ to $|--\rangle$, and hence states $|+-\rangle$, $| -+\rangle$ remain out of the ground state manifold.

as depicted in Fig. 6. Each of the four vertical wires $n = 1, \dots, 4$ is coupled to each of the four horizontal wires $i = 1, \dots, 4$ by a Josephson junction. The sign of each coupling is encapsulated by a matrix W with diagonal elements $W_{n=i} = -1$ (corresponding to a π -junction) and off-diagonal elements $W_{n \neq i} = +1$ (corresponding to a regular junction).

The Hamiltonian at a given site s for such a system is given by

$$H = H_J + H_K \quad (18a)$$

with

$$H_J = -J \sum_{n,i} W_{ni} \cos(\phi_n - \theta_i) \quad (18b)$$

and

$$H_K = \frac{1}{2C_m} \sum_n q_n^2 + \frac{1}{2C_g} \sum_i Q_i^2, \quad (18c)$$

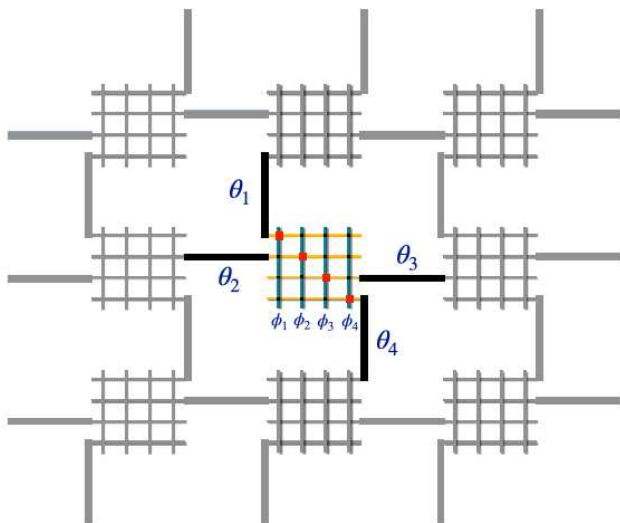


FIG. 6. A proposed physical realization of the star term \mathcal{A}_s in the $U(1)$ toric code lattice Hamiltonian. The center “waffle” is highlighted as an example. It is composed of intersecting superconducting wires coupled by Josephson junctions. The junctions in the diagonal (red) denote π couplings. Vertical wires (blue) are “matter” degrees of freedom labeled by phase ϕ_n . Horizontal wires (gold) are “gauge” degrees of freedom with phases θ_i . Only the gauge degrees of freedom (black) couple to other, neighboring, waffles.

where C_m and C_g are the self-capacitances. ϕ_n and θ_i are the superconducting phases in each wire and q_n and Q_i are their conjugate charges, respectively. On the lattice, we refer to the ϕ as “matter” phases and they are not connected to wires on any other site. On the other hand, we refer to the θ as “gauge” phases and they are shared by neighboring sites. (Here we focus on a single star; on a lattice, gauge wires are shared between neighboring stars.)

The form of the W -matrix guarantees that this Hamiltonian has local \mathbb{Z}_2 symmetry, per combinatorial gauge symmetry (CGS). At the same time, this Hamiltonian also has global $U(1)$ symmetry, hence it is a natural starting point for the $U(1)$ toric code.

There are two types of limits that one usually considers in Josephson junction Hamiltonians – phase and charge. The former is dominated by large J where the flux is typically treated classically and then one considers the quantum fluctuations perturbatively. We are interested in the opposite charging limit, where both capacitances are small and we are in the quantum regime at the outset. To treat this case we will proceed in two steps: first take the limit of small C_m and then small C_g .

Small C_m limit: first, we add a bias voltage \bar{q} to each matter wire so that the kinetic term becomes

$$\frac{1}{2C_m} (q_n - \bar{q})^2. \quad (19)$$

If the bias is close to $\bar{q} = N + 1/2$ (N is an integer) such that two quantized states $q_n = N$ and $q_n = N + 1$

are close in energy, then the matter wires become two-level systems, because the small capacitance penalizes all other charge states. For our purposes we consider a gate bias very close to the half integer point. At this point the operators $e^{\pm i\phi_n}$ increase or decrease the charge value and we can replace them by ordinary spin raising/lowering operators $e^{\pm i\phi_n} \rightarrow \mu_n^{\pm}$, where $\mu_n^{\pm} = \mu_n^x \pm i\mu_n^y$. [84]. The Hamiltonian (18b) in this limit becomes

$$H_J = -J \sum_{n,i} W_{ni} (\mu_n^+ e^{+i\theta_i} + \mu_n^- e^{-i\theta_i}). \quad (20)$$

The μ spins can be integrated out exactly by diagonalizing, for each n , a 2×2 spin-1/2 Hamiltonian (treating the θ_i 's as slow fields). Keeping only the lowest energy terms, the result is an effective potential as a function of θ_i 's only:

$$H_J^{\text{eff}} = -|J| \sum_n \left[\sum_{i,j} W_{ni} W_{nj} \cos(\theta_i - \theta_j) \right]^{1/2}. \quad (21)$$

Notice that this Hamiltonian still has the global $U(1)$ symmetry as well as the discrete \mathbb{Z}_2 symmetry, which we can write as:

$$\theta_i \rightarrow \theta_i + \frac{\pi}{2} (1 - \sigma_i^z), \quad \sigma_i^z = \pm 1, \quad \text{if } \sigma_1^z \sigma_2^z \sigma_3^z \sigma_4^z = +1. \quad (22)$$

Small C_g limit: now we will follow a similar procedure with the gauge wires and add a bias $\bar{Q} = M + 1/2$ (M is an integer) to all Q_i . This restricts the charge on each gauge wire to two values.

Mathematically, however, we take a different approach. Rather than replacing the flux operators by Pauli matrices immediately, we will first expand Eq. (21) in a Fourier series, keeping only the terms $e^{\pm i\theta_i}$, i.e., those that change the charge from one to zero or vice versa on each wire. It is straightforward to check that the only terms that appear in the Fourier expansion have the form of \mathcal{A}_s in Eq. (4) but with each spin operator σ_i^{\pm} standing for $e^{\pm i\theta_i}$.

We note that this procedure realizes the star term \mathcal{A}_s , but we do not generate the plaquette term B_p . It remains a problem for future work to systematically study different sectors with given eigenvalues of B_p to determine whether the ground states of Hamiltonian Eq. (7) with $\lambda_B = 0$ remain those in the sector with $B_p = +1$ for all p , which were justified in our Quantum Monte Carlo studies by the presence of the sufficiently large λ_B coupling in the Hamiltonian.

VI. CONCLUSIONS

In this work, we studied a spin-1/2 lattice model – the $U(1)$ toric code – that is invariant under both a global $U(1)$ symmetry and local \mathbb{Z}_2 gauge transformations. We presented evidence that the system is gapped and the

$U(1)$ global symmetry is not spontaneously broken. The exponential decay of spin-spin correlators support the claim that the system is a gapped spin liquid. We found topologically degenerate ground states, labeled by non-contractible string operators.

The model displays quite distinct topological degeneracies that depend on the tilt of the lattice that is wrapped around the torus, a form of UV/IR mixing unlike those encountered, for example, in fractonic models. The number of degenerate ground states is also puzzling. It is difficult to explain the three-fold topological degeneracy for the 45° -tilt compactification as coming from Abelian topological order if the $U(1)$ toric code is described by a doubled theory (for example, the usual toric code which is described by a doubled Chern-Simons theory).

One logical possibility is that the enrichment of the Z_2 toric code by the global $U(1)$ symmetry may turn the topological order non-Abelian. We presented an heuristic argument aimed at relating the three-fold topological degeneracy for the 45° -tilt compactification to the two-fold topological degeneracy for the 0° -tilt compactification based on a mapping of posited logical operators that switch between topological ground states in both geometries.

Finally, we presented a physical realization of the $U(1)$ -symmetric star terms in the Hamiltonian in a system of superconducting quantum wires coupled by Josephson junctions at their crossings. We believe that the possibility that the model may be realizable with physical Hamiltonians should further motivate future theoretical studies of the unusual topological properties of the $U(1)$ toric code.

ACKNOWLEDGMENTS

We thank Anders Sandvik for enlightening discussions and valuable comments. The work of K.-H.W., A.K., G.D., and C.C. is partially supported by the DOE Grant DE-FG02-06ER46316 (work on designing topological phases of matter and foundations of combinatorial gauge theory) and by the NSF Grant DMR-1906325 (work on interfaced topological states in superconducting wires).

Appendix A: Hilbert space fragmentation

A symmetry operator \hat{O} , one that commutes with the Hamiltonian, block-diagonalizes the Hamiltonian into symmetry sectors associated with quantum numbers, i.e., eigenvalues of \hat{O} .

Sometimes, even after resolving all symmetries of the model, a symmetry block might appear to be further block-diagonalized into smaller blocks that are not associated with any obvious symmetry operators. This phenomenon is called Hilbert space fragmentation and the corresponding (quantum) dynamically disconnected

blocks are called Hilbert space fragments or Krylov subsectors [70–72]. In the thermodynamic limit, the number of Krylov subsectors originating from Hilbert space fragmentation scales much faster (proportional to the number of degrees of freedom) than the number of symmetry sectors from any type of symmetry (unless it is a local gauge symmetry) [72]. The corresponding conserved operators (which can be constructed, e.g., by writing down a projector on the observed block in the Hamiltonian) are highly non-local and non-trivial.

Hilbert space fragmentation typically arises in models with local kinetic constraints. Such constraints are present in the $U(1)$ toric code. As an example, consider the two states in Fig. 7. They belong to the same symmetry sector. Namely, they belong to the block with quantum numbers: $M_z = 0$, $W_x = W_y = +1$, $B_p = +1$ for every plaquette p . However, the state at the top is completely inert, since none of the stars are flippable, while in the state at the bottom every star is flippable. These states are dynamically disconnected and belong to different Krylov subsectors. In fact, the inert state comprises its own 1-dimensional Krylov subsector. Another example of a 7-dimensional Krylov subsector is shown in Fig. 7(b). If we translate this pattern of spins in space, we will obtain a different Krylov subsector with the same quantum numbers.

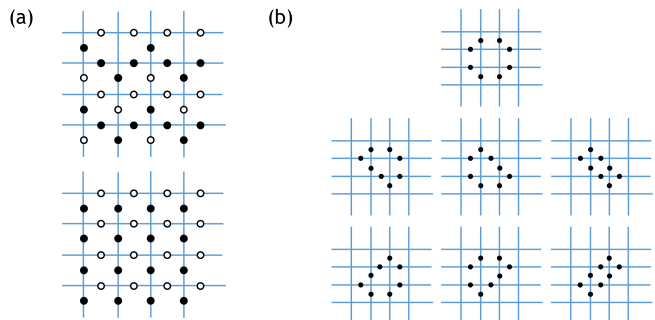


FIG. 7. (a) Two states from the same symmetry sector, but from different Krylov subsectors: an inert state with no flippable stars (top), and a state where every star is flippable (bottom) (b) Basis states of a 7-dimensional Krylov subsector. Black dots denote spin-downs, white dots (or the absence of a dot) denote spin-ups.

Hilbert space fragmentation in a model that straightforwardly maps to the topological $(+, +)$ sector of the $U(1)$ toric code has been studied in works [73, 76]. Dynamics of domain walls in the same setting has been studied in [74, 75].

Using explicit enumeration of states, we study Hilbert space fragmentation in systems of size $N = 4 \times 4 \times 2, 6 \times 4 \times 2$ and $8 \times 4 \times 2$ (the first two numbers are the numbers of stars in x - and y -directions, the last factor of 2 corresponds to the two spins in a unit cell). We concentrate on the symmetry sector with all $B_p = +1$. We define D_{\max} as the dimensionality of the largest Krylov subsector and D as the dimensionality of the corresponding symmetry

sector. The ratio of D_{\max}/D for different magnetization and topological symmetry sectors is presented in Fig. 8.

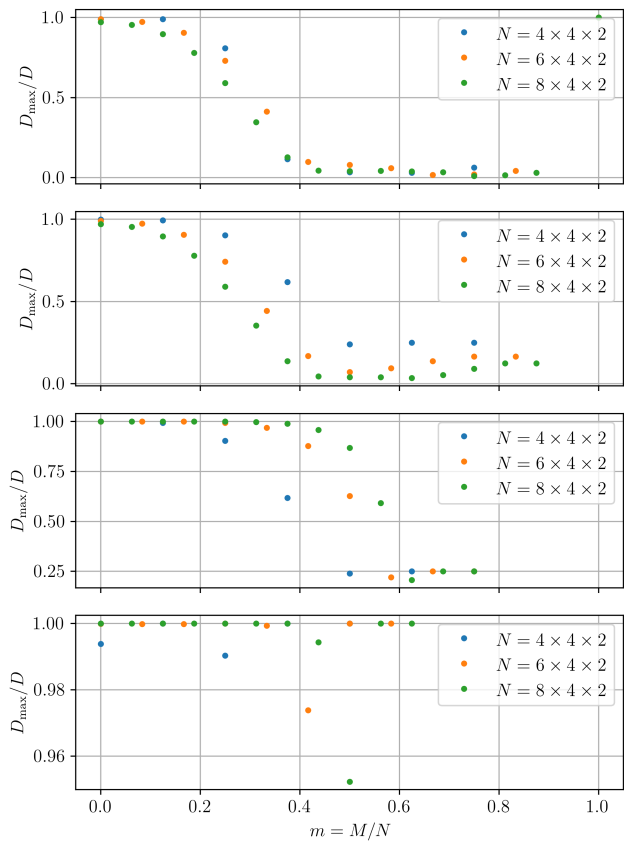


FIG. 8. Exact enumeration study of the fragmentation fraction defined as D_{\max}/D , where D_{\max} is the size of the largest fragment, and D is the size of the sector. From top to bottom are the $(+, +)$, $(+, -)$, $(-, +)$ and $(-, -)$ topological sectors, respectively.

One can see that in the vicinity of zero magnetization, the largest Krylov subsector completely dominates the Hilbert space of its symmetry sector. We conjecture that this behavior carries over to the thermodynamic limit. In addition, by a simple combinatorial argument, it is apparent that the largest symmetry sectors are with $M_z = 0$. Since larger random matrices have a larger spread of eigenvalues than smaller random matrices, we can safely assume that the ground state of each of the four topological symmetry sectors belongs to its largest Krylov subsector in the $M_z = 0$ sector. Work [73] proves this with even more rigor, although their results translate directly only to our $(+, +)$ topological sector. In addition, we confirm the results of [73] by observing the same “dynamical freezing transition”, which can be seen as a sharp drop of the D_{\max}/D value at intermediate values of magnetization [except for the $(-, -)$ sector; however, this might be a finite size effect].

Appendix B: Generalized sweeping cluster update algorithm

The model we consider does not have a sign problem. Therefore, a QMC simulation is possible. We employ the SSE QMC with a modification of the sweeping cluster update algorithm, previously used to study the quantum dimer model [79, 85].

As it is typically done in the SSE simulations, the partition function is expanded in a series of powers of the Hamiltonian H . Terms from this series are sampled as classical configurations, where slices of “imaginary time” contain “vertices” that take one local classical configuration to another one, according to one of the terms in the Hamiltonian. For a comprehensive review of the SSE, see [78]. In the $U(1)$ toric code, there are only 6 allowed off-diagonal vertices with equal weight, as shown in Fig. 9(a). In order to perform the simulation, all diagonal terms have to be non-zero. To achieve this, we add a constant to the Hamiltonian, which then allows additional 16 diagonal vertices as shown in Fig. 9(b). The constant is chosen such that all the vertices have equal weight. Vertices with 2-up-2-down configurations are called “flippable stars”, as marked by green frames in Fig. 9. In the following, we set the weight of all vertices to 1.

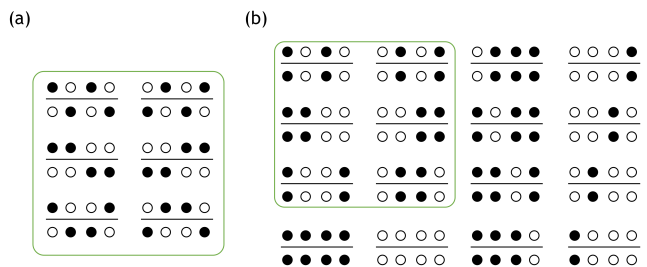


FIG. 9. (a) 6 allowed off-diagonal vertices from the Hamiltonian. Black (white) dots denote spin-up (spin-down). The four dots below (above) the line denote the classical configuration of the four spins on a star before (after) the application of a Hamiltonian term. (b) 16 additional allowed diagonal vertices after adding a constant to the Hamiltonian. The 12 vertices marked by green frames are the flippable stars.

Each Monte Carlo step consists of two parts. First, the standard diagonal update is performed. If an “imaginary time” slice is empty, then a diagonal operator on a random star might be inserted; if an “imaginary time” already contains a diagonal operator, then it might be removed. The probabilities of these two processes are

$$P_{\text{insert}} = \frac{\beta N_s}{(M - n)}, \quad (B1)$$

$$P_{\text{remove}} = \frac{(M - n + 1)}{\beta N_s}.$$

Here, $\beta = 1/T$ is the inverse temperature, $N_s = L_x \times L_y$ is the total number of stars, M is the total length of

the operator-string (i.e., the number of “imaginary time” slices), and n is the total number of non-identity operators present in the current operator-string. Off-diagonal operators are left untouched during this step.

After the diagonal update, a sweeping cluster update is performed. The construction of a cluster starts with randomly choosing a flippable star, either diagonal or off-diagonal. This creates 4 defect lines, which propagate upward along the “imaginary time” direction and start growing the cluster. We then sweep over “imaginary time” slices, and keep track of the defect lines. If a vertex is hit by one or more defect lines, we update the vertex according to specific rules and propagate the defect lines further. The number of defect lines exiting a vertex might be different from how many defect lines entered it. At some point, the cluster will converge and the defect lines will terminate at another flippable star. The pictorial representation of a cluster is shown in Fig. 10. We note that the case in which a vertex has a different

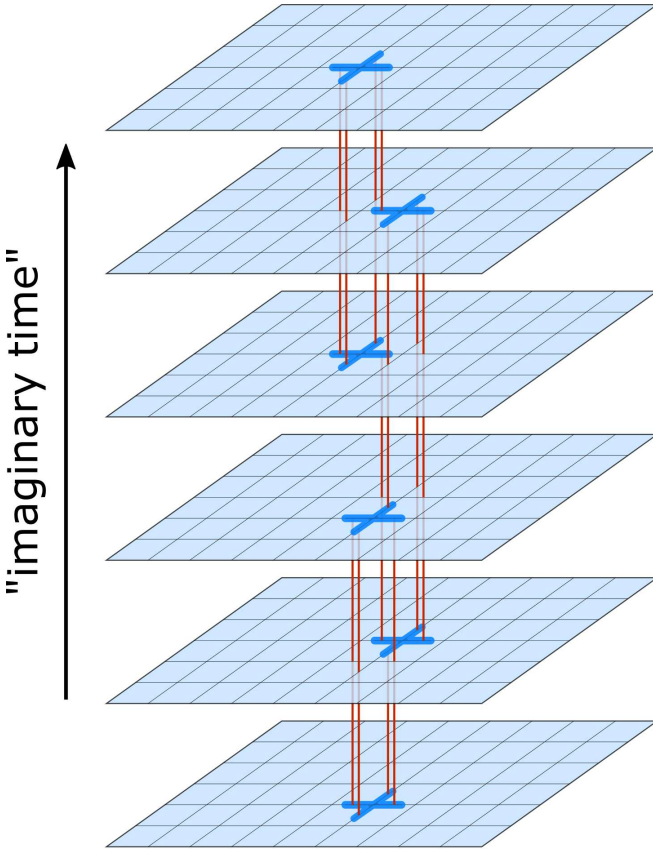


FIG. 10. Example of a cluster. It starts as 4 defect lines coming out of a flippable star. The defect lines propagate upward along the “imaginary time” direction, modifying the vertices they encounter according to specified rules. After a vertex, the number of defect lines might potentially increase/decrease. Finally, the cluster terminates at another flippable star.

numbers of entering and exiting lines has been explored in Ref. 85 using a different approach. Our model (as well

as the dimer model) has a special property that allows the cluster to build in one directional.

To determine the rules for the vertex updates, we proceed in the following way. Consider a vertex that is hit by some number of defect lines from below. We flip the corresponding spins and obtain an intermediate vertex configuration, as shown in Fig. 11. At this point, there are four possibilities:

1. If the configuration of the bottom four spins of an intermediate vertex is non-flippable, then there is only one way to propagate the defect lines through the vertex. Some examples are shown in Fig. 11(a).
2. If the defect lines flip the bottom four spins into a flippable configuration, and there are less than 4 lines hitting the vertex, then there are two possible ways to propagate the defect lines. The resulting vertex can be either diagonal or off-diagonal, with probability 1/2 each. Examples are shown in Fig. 11(b).
3. If 4 defect lines hit a flippable vertex and the total number of defect lines is more than 4, then we propagate all the lines and flip the entire vertex.
4. If 4 defect lines hit a flippable vertex and the total number of defect lines is exactly 4, then we terminate the cluster.

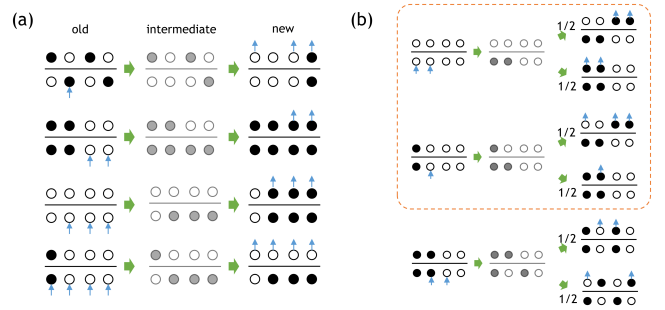


FIG. 11. Examples of vertex updates. Blue arrows denote the defect lines propagating along the “imaginary time” direction (from bottom to top). (a) If a new configuration of the bottom four spins is not flippable, there is a unique way to propagate the defect lines, such that the new vertex remains allowed. (b) If less than 4 defect lines hit a vertex and update the bottom four spins to a flippable configuration, there are two possible ways to propagate the defect lines. We choose one of them with probability 1/2. Processes marked by the orange frame are the updates from a non-flippable vertex to a flippable vertex, for which the reverse process does not have probability 1/2.

Note that the update from a non-flippable vertex to a flippable vertex has probability 1/2, while the reverse process does not. Thus, to satisfy the detail balance, we have to keep track of how many times these processes occur. Consider an operator-string A that updates to an

operator-string B through a flip of a cluster constructed using the aforementioned procedure. During this update, the number of non-flippable vertices that turned into flippable ones is $N_{n \rightarrow f}$, while the number of flippable vertices that turned into non-flippable ones is $N_{f \rightarrow n}$. To satisfy detailed balance, the acceptance probability for the process $A \rightarrow B$ (through the flip of the constructed cluster) should then be

$$P(A \rightarrow B) = \frac{N_v(A)}{N_v(B)} \left(\frac{1}{2}\right)^{N_{f \rightarrow n} - N_{n \rightarrow f}}, \quad (\text{B2})$$

where N_v is the number of flippable vertices present in the corresponding operator-string.

It is worth pointing out that the update procedure we described conserves all quantum numbers, $\{M_z, W_x, W_y, \{B_p\}\}$. Even more than that, the update procedure cannot take the system out of a specific Hilbert space fragment (Krylov subsector). In this way, by choosing an appropriate initial state, we are able to target a Hilbert space fragment that is dynamically connected to that initial state. As we explain in Appendix A, in the vicinity of zero magnetization, the Hilbert space of symmetry sectors is dominated by a single large fragment, which will most probably contain the lowest energy eigenstate. We benchmark our QMC results by comparing them to the results obtained from an ED calculation of a small system size. The results are presented in Fig. 12.

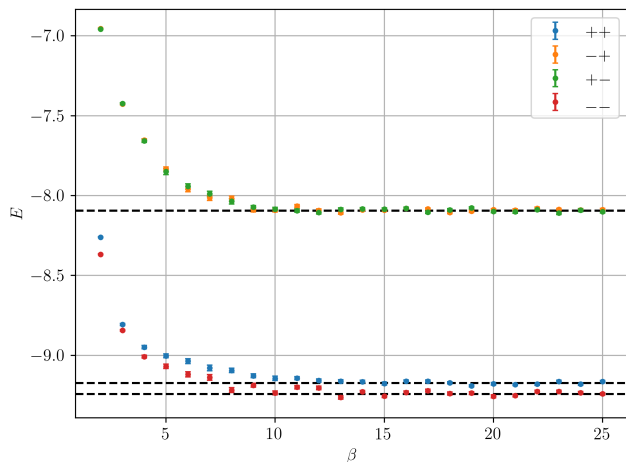


FIG. 12. Ground state energy in four topological sectors of a system of size 4×4 stars. (dots) obtained from the SSE QMC with the generalized sweeping cluster update algorithm; (dashed lines) obtained from the ED calculation.

Appendix C: Energies in different magnetization sectors

For a system with size $L_x \times L_y$ on a square lattice, there are $2^{L_x L_y + 1}$ sectors associated to the \mathbb{Z}_2 plaquette

operators, $(2L_x L_y + 1)$ sectors associated to the global $U(1)$ symmetry, and 4 sectors associated to the string operators $W_{x,y}$. However, not all of these sectors have states (i.e., they are of non-zero dimension.)

For example, in a system with L even, the sector with $\{B_p = +1\}$ and $(W_x, W_y) = (+, +)$ is incompatible with odd magnetization $M_z = \pm 1, \pm 3, \pm 5, \pm 7, \pm 9, \dots$, meaning that such sectors have vanishing dimension, or equivalently, they are non-existent. Conversely, in a system with L odd, all sectors with $\{B_p = +1\}$ and $(W_x, W_y) = (+, +)$ can only have odd magnetization, and consequently all even magnetization sectors vanish.

In Fig. 13, we show the difference in energy between the lowest states in each magnetization sector and the lowest state with $M_z = 0$, within the topological sector $(+, +)$. The results indicate that the state with $M_z = 0$ has the lowest energy.

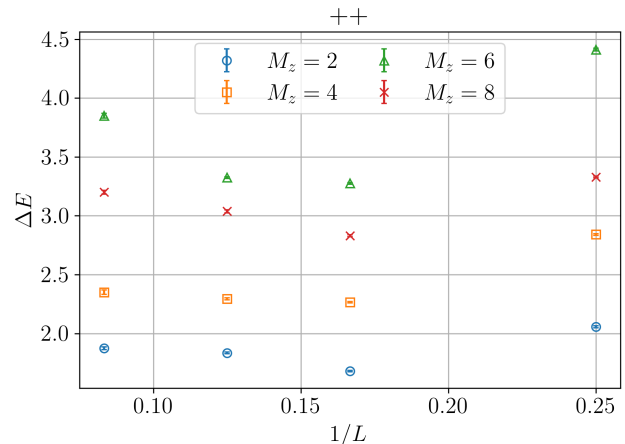


FIG. 13. Energy differences between the lowest states with total magnetization $M_z = 2, 4, 6, 8$ and the lowest state with magnetization $M_z = 0$, within the $(+, +)$ sector, as a function of inverse system size $1/L$. The system has 45° -tilt compactification.

Appendix D: Spin-spin correlation functions in different sectors for 0° and 45° compactifications

The spin-spin correlation functions in Eq. (13) were presented for the $(-, -)$ sector and for 0° -tilt compactification in Fig. 3.

We show in Fig. 14 the QMC results for spin-spin correlations obtained in the other topological sectors, $(+, +)$ and $(+, -)$, for 0° -tilt compactification. [The results for the sectors $(+, -)$ and $(-, +)$ are identical by symmetry.] The data shows a rapid decay of correlations in all topological sectors.

In Fig. 15, we present the spin-spin correlation functions for 45° -tilt compactification, for all topological sectors. We again observe rapidly decaying spatial correla-

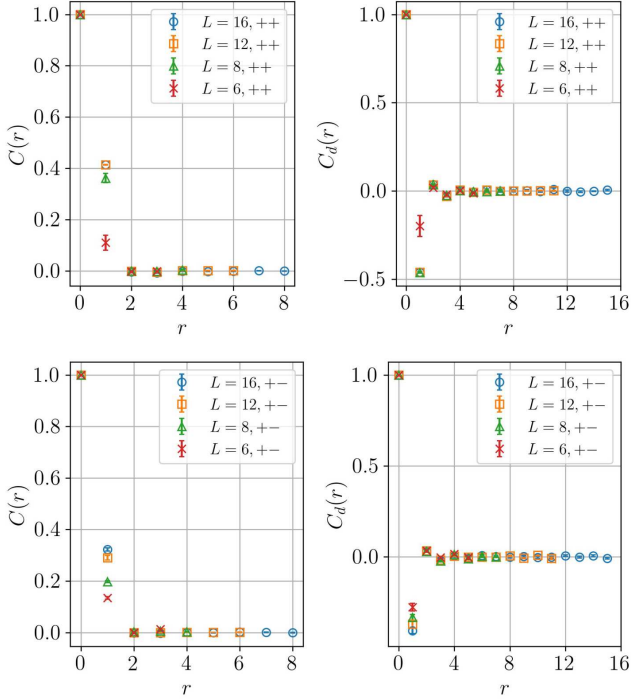


FIG. 14. Spin-spin correlation functions in sectors $(+, +)$ (upper two figures) and $(+, -)$ (lower two figures) for 0° -tilt compactification. The correlations decay to zero for distances of the order of two lattice sites.

tions, consistent with the absence of long range magnetic order.

In the 45° -tilt compactification scheme we also observe that the star-star correlators $\langle \mathcal{A}_s \mathcal{A}_{s'} \rangle$ present a staggered pattern, similar to what we observed for the 0° -tilt case and showed in Fig. 3. This provides evidence that within each topological sector we have a two-fold degeneracy associated to spontaneous translational symmetry breaking. Accounting for this additional factor of 2, the total ground state space is 6-fold degenerate. (Note that this additional degeneracy is not topological and can be lifted by local perturbations.)

Appendix E: Odd system sizes results for 0° and 45° compactifications

In Fig. 16, we show the QMC results of energy in 4 different topological sectors with odd system size L on both the 0° and 45° compactifications.

With odd system size L , as shown in Fig. 16(a) for the case of 0° -tilt, we find that sectors $(+, +)$ and $(-, -)$ are not compatible with even magnetization. Therefore, the lowest energy levels in these sectors has $M_z = \pm 1$, not $M_z = 0$. These states can be split by a local longitudinal field perturbation term in the Hamiltonian. On the other hand, sectors with $(+, -)$ and $(-, +)$ are compatible with even magnetization, and the lowest energy states have

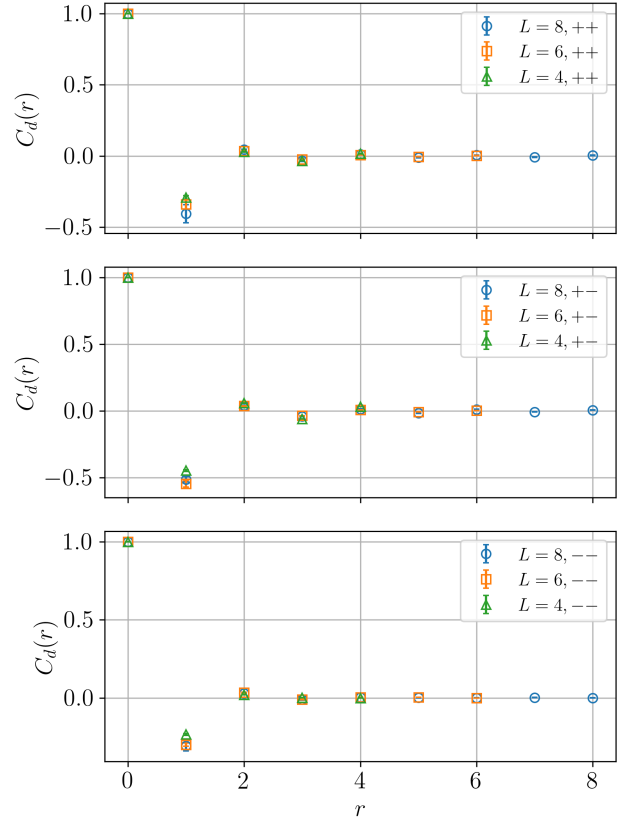


FIG. 15. Spin-spin correlation functions in the topological sectors $(+, +)$, $(+, -)/(-, +)$ and $(-, -)$ for the 45° -tilt setup. All the results shows a fast decaying within the order of two lattice sites for all system sizes L .

$M_z = 0$. Based on the above observation, we believe that in case the topological order is present in the system, the TGSD has to come from the $(+, -)$ and $(-, +)$ sectors.

In the case of 45° -tilt, all four topological sectors are compatible with even magnetization and the lowest energy states have $M_z = 0$. As shown in Fig. 16(b), we find that states from $(+, -)$, $(-, +)$ and $(-, -)$ become degenerate at low temperatures ($\beta = 1/T$), indicating a three-fold TGSD. Compared to the even L case, the TGSD stays the same, but instead of the $(+, +)$ sector, the reference sector is now $(-, -)$.

Appendix F: ED results for other compactifications

For other compactification schemes, we study the ground state energy in different topological sectors using ED (see Fig. 17). The total number of stars is $N_s = (a^2 + b^2)L^2$, and the total number of spins is $N = 2N_s$. Here, we show the results only for zero magnetization, as we find that the states with $M_z = 0$ have lower energy than other states non-zero magnetization states.

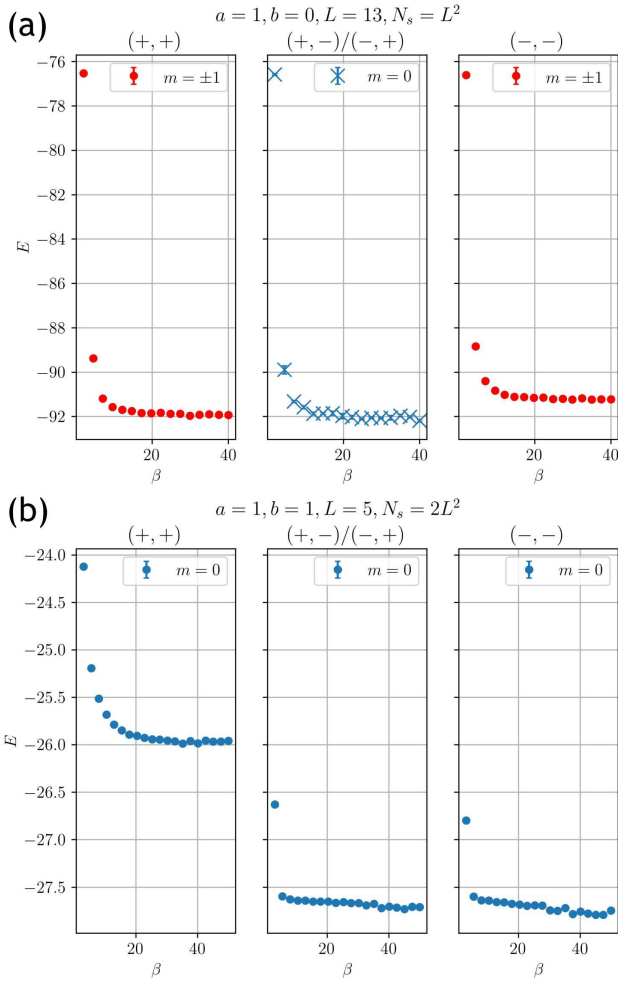


FIG. 16. QMC results of energies in 4 topological sectors for (a) 0° -tilt with system size $L = 13$ where only the sectors $(+,-)$ and $(-,+)$ are compatible with zero magnetization. (b) 45° -tilt with system size $L = 5$, where the TGSD remains three as the even size system, but the degenerate sectors are $(+,-)$, $(-,+)$ and $(-,-)$. N_s denotes the total number of stars on the lattice.

Due to size limitations to the computations, it is only possible to study compactification schemes with small values of a and b . Here we show results for three different cases: a) $a = 2, b = 1$ and $L = 2$ ($N_s = 20$); b) $a = 3, b = 1$ and $L = 1$ ($N_s = 10$); and c) $a = 3, b = 2$ and $L = 1$ ($N_s = 13$). In case (a), we find energy features similar to the 0° -tilt case with an even system size L . The lowest energy states of sectors $(+,+)$ and $(-,-)$ are

well separated from the lowest energy states of $(+,-)$ and $(-,+)$ sectors, and are, possibly, the two topologically degenerate ground states, with the small energy difference between them being a finite size effect. Likewise, for (b), we find that the energies behave similarly to the 45° -tilt case. The $(+,-)$, $(-,+)$ and $(-,-)$ sectors contain the 3 topologically degenerate ground states, again, separated by a small finite size gap and well separated from the $(+,+)$ sector. In case (c), sectors $(+,+)$ and $(-,-)$ are incompatible with even magnetization, and states from the $(+,-)$, $(-,+)$ sectors are degenerate, similarly to the 0° -tilt case with odd system size L .

Based on the above observations, we find that the TGSD is always either 2 or 3, depending on the compactification scheme. The results can be summarized in the following way: if $(a^2 + b^2)$ is even, $\text{TGSD} = 3$; if $(a^2 + b^2)$ is odd, $\text{TGSD} = 2$. In the case of $\text{TGSD} = 3$, if L is even, the ground states belong to the $(+,+)$, $(+,-)$, $(-,+)$ sectors, while if L is odd, they belong to the $(-,-)$, $(+,-)$, $(-,+)$ sectors. In the case of $\text{TGSD} = 2$, for even L , the ground states lie in the $(+,+)$ and $(-,-)$ sectors, while for odd L , the $(+,+)$ and $(-,-)$ sectors are not compatible with zero magnetization and the ground states lie in sectors $(+,-)$, $(-,+)$.

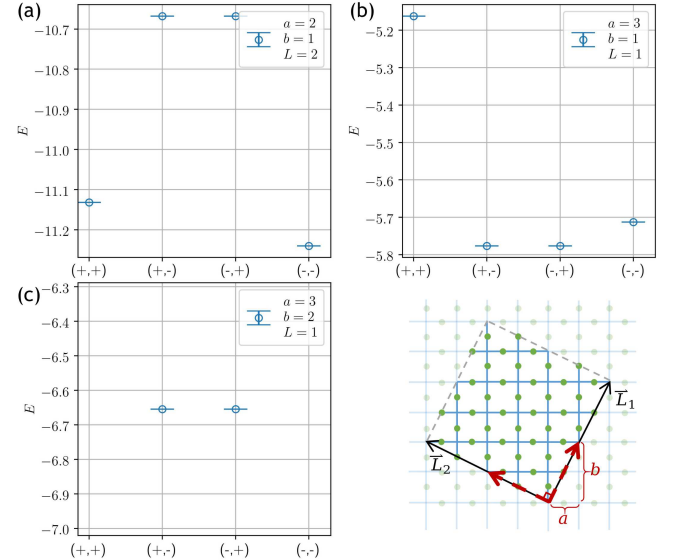


FIG. 17. ED results for the energy of the lowest states in each topological sector with $m = 0$ for different compactifications. (a) $a = 2, b = 1, L = 2$. (b) $a = 3, b = 1, L = 1$ (c) $a = 3, b = 2, L = 1$.

[1] X.-G. Wen, *International Scholarly Research Notices* **2013** (2013).
 [2] F. J. Wegner, *Journal of Mathematical Physics* **12**, 2259 (1971).
 [3] X. G. Wen, *Phys. Rev. B* **40**, 7387 (1989).

[4] X. G. Wen, *International Journal of Modern Physics B* **04**, 239 (1990), <https://doi.org/10.1142/S0217979290000139>.
 [5] X. G. Wen and Q. Niu, *Phys. Rev. B* **41**, 9377 (1990).
 [6] D. P. Arovas, R. Schrieffer, F. Wilczek, and A. Zee,

- Nuclear Physics B **251**, 117 (1985).
- [7] F. Wilczek, *Phys. Rev. Lett.* **69**, 132 (1992).
- [8] A. Kitaev, *Annals of Physics* **303**, 2 (2003).
- [9] A. Kitaev, *Annals of Physics* **321**, 2 (2006), January Special Issue.
- [10] A. Stern, *Annals of Physics* **323**, 204 (2008), January Special Issue 2008.
- [11] N. Read and B. Chakraborty, *Phys. Rev. B* **40**, 7133 (1989).
- [12] N. Read and S. Sachdev, *Phys. Rev. Lett.* **66**, 1773 (1991).
- [13] X. G. Wen, *Phys. Rev. B* **44**, 2664 (1991).
- [14] L. Balents, M. P. A. Fisher, and C. Nayak, *Phys. Rev. B* **60**, 1654 (1999).
- [15] T. Senthil and M. P. A. Fisher, *Phys. Rev. B* **62**, 7850 (2000).
- [16] R. Moessner and S. L. Sondhi, *Phys. Rev. Lett.* **86**, 1881 (2001).
- [17] R. Moessner, S. L. Sondhi, and E. Fradkin, *Phys. Rev. B* **65**, 024504 (2001).
- [18] L. Balents, M. P. A. Fisher, and S. M. Girvin, *Phys. Rev. B* **65**, 224412 (2002).
- [19] M. A. Levin and X.-G. Wen, *Phys. Rev. B* **71**, 045110 (2005).
- [20] L. Savary and L. Balents, *Reports on Progress in Physics* **80**, 016502 (2016).
- [21] C. Broholm, R. J. Cava, S. A. Kivelson, D. G. Nocera, M. R. Norman, and T. Senthil, *Science* **367**, eaay0668 (2020), <https://www.science.org/doi/pdf/10.1126/science.aay0668>.
- [22] D. C. Tsui, H. L. Stormer, and A. C. Gossard, *Phys. Rev. Lett.* **48**, 1559 (1982).
- [23] R. B. Laughlin, *Phys. Rev. Lett.* **50**, 1395 (1983).
- [24] S. C. Zhang, T. H. Hansson, and S. Kivelson, *Phys. Rev. Lett.* **62**, 82 (1989).
- [25] T. Hansson, V. Oganesyan, and S. Sondhi, *Annals of Physics* **313**, 497 (2004).
- [26] E. Witten, *Commun. Math. Phys.* **117**, 353 (1988).
- [27] E. Witten, *Commun. Math. Phys.* **121**, 351 (1989).
- [28] C. Chamon, *Phys. Rev. Lett.* **94**, 040402 (2005).
- [29] S. Bravyi, B. Leemhuis, and B. M. Terhal, *Annals of Physics* **326**, 839 (2011).
- [30] J. Haah, *Phys. Rev. A* **83**, 042330 (2011).
- [31] B. Yoshida, *Phys. Rev. B* **88**, 125122 (2013).
- [32] J. Haah, *Communications in Mathematical Physics* **324**, 351 (2013).
- [33] S. Vijay, J. Haah, and L. Fu, *Phys. Rev. B* **92**, 235136 (2015).
- [34] S. Vijay, J. Haah, and L. Fu, *Phys. Rev. B* **94**, 235157 (2016).
- [35] M. Pretko, X. Chen, and Y. You, *International Journal of Modern Physics A* **35**, 2030003 (2020), <https://doi.org/10.1142/S0217751X20300033>.
- [36] N. Seiberg and S.-H. Shao, *SciPost Phys.* **10**, 027 (2021).
- [37] N. Seiberg and S.-H. Shao, *SciPost Phys.* **9**, 046 (2020).
- [38] C. L. Kane and E. J. Mele, *Phys. Rev. Lett.* **95**, 226801 (2005).
- [39] C. L. Kane and E. J. Mele, *Phys. Rev. Lett.* **95**, 146802 (2005).
- [40] B. A. Bernevig, T. L. Hughes, and S.-C. Zhang, *Science* **314**, 1757 (2006), <https://www.science.org/doi/pdf/10.1126/science.1133734>.
- [41] J. E. Moore and L. Balents, *Phys. Rev. B* **75**, 121306 (2007).
- [42] L. Fu, C. L. Kane, and E. J. Mele, *Phys. Rev. Lett.* **98**, 106803 (2007).
- [43] R. Roy, *Phys. Rev. B* **79**, 195322 (2009).
- [44] Y. Ando, *Journal of the Physical Society of Japan* **82**, 102001 (2013), <https://doi.org/10.7566/JPSJ.82.102001>.
- [45] M. Sato and Y. Ando, *Reports on Progress in Physics* **80**, 076501 (2017).
- [46] W. P. Su, J. R. Schrieffer, and A. J. Heeger, *Phys. Rev. Lett.* **42**, 1698 (1979).
- [47] F. Haldane, *Physics Letters A* **93**, 464 (1983).
- [48] I. Affleck, T. Kennedy, E. H. Lieb, and H. Tasaki, *Phys. Rev. Lett.* **59**, 799 (1987).
- [49] X. Chen, Z.-C. Gu, Z.-X. Liu, and X.-G. Wen, *Science* **338**, 1604 (2012), <https://www.science.org/doi/pdf/10.1126/science.1227224>.
- [50] X.-G. Wen, *Phys. Rev. B* **65**, 165113 (2002).
- [51] M. Levin and A. Stern, *Phys. Rev. B* **86**, 115131 (2012).
- [52] A. M. Essin and M. Hermele, *Phys. Rev. B* **87**, 104406 (2013).
- [53] L.-Y. Hung and X.-G. Wen, *Phys. Rev. B* **87**, 165107 (2013).
- [54] A. Meszaros and Y. Ran, *Phys. Rev. B* **87**, 155115 (2013).
- [55] C.-Y. Huang, X. Chen, and F. Pollmann, *Phys. Rev. B* **90**, 045142 (2014).
- [56] Y.-M. Lu and A. Vishwanath, *Phys. Rev. B* **93**, 155121 (2016).
- [57] M. Cheng, Z.-C. Gu, S. Jiang, and Y. Qi, *Phys. Rev. B* **96**, 115107 (2017).
- [58] Q.-R. Wang and M. Cheng, *Phys. Rev. B* **106**, 115104 (2022).
- [59] A. Kitaev, *AIP Conference Proceedings* **1134**, 22 (2009), <https://aip.scitation.org/doi/pdf/10.1063/1.3149495>.
- [60] X. Chen, F. J. Burnell, A. Vishwanath, and L. Fidkowski, *Phys. Rev. X* **5**, 041013 (2015).
- [61] N. Tarantino, N. H. Lindner, and L. Fidkowski, *New Journal of Physics* **18**, 035006 (2016).
- [62] M. Barkeshli, P. Bonderson, M. Cheng, and Z. Wang, *Phys. Rev. B* **100**, 115147 (2019).
- [63] M. Levin, F. J. Burnell, M. Koch-Janusz, and A. Stern, *Phys. Rev. B* **84**, 235145 (2011).
- [64] C. Chamon, D. Green, and A. J. Kerman, *PRX Quantum* **2**, 030341 (2021).
- [65] C. Chamon, D. Green, and Z.-C. Yang, *Phys. Rev. Lett.* **125**, 067203 (2020).
- [66] K.-H. Wu, Z.-C. Yang, D. Green, A. W. Sandvik, and C. Chamon, *Phys. Rev. B* **104**, 085145 (2021).
- [67] D. Green and C. Chamon, *arXiv preprint arXiv:2209.14333* (2022).
- [68] H. Yu, G. Goldstein, D. Green, A. E. Ruckenstein, and C. Chamon, *arXiv preprint arXiv:2212.03880* (2022).
- [69] T. Rudelius, N. Seiberg, and S.-H. Shao, *Phys. Rev. B* **103**, 195113 (2021).
- [70] V. Khemani, M. Hermele, and R. Nandkishore, *Phys. Rev. B* **101**, 174204 (2020).
- [71] P. Sala, T. Rakovszky, R. Verresen, M. Knap, and F. Pollmann, *Phys. Rev. X* **10**, 011047 (2020).
- [72] S. Moudgalya and O. I. Motrunich, *Phys. Rev. X* **12**, 011050 (2022).
- [73] O. Hart and R. Nandkishore, (2022), [10.48550/ARXIV.2203.06188](https://arxiv.org/abs/10.48550/ARXIV.2203.06188).
- [74] F. Balducci, A. Gambassi, A. Leroche, A. Scardicchio, and C. Vanoni, *arXiv preprint arXiv:2203.09495* (2022).
- [75] F. Balducci, A. Gambassi, A. Leroche, A. Scardicchio, and C. Vanoni, *arXiv preprint arXiv:2209.08992* (2022).

- [76] A. Yoshinaga, H. Hakoshima, T. Imoto, Y. Matsuzaki, and R. Hamazaki, *Phys. Rev. Lett.* **129**, 090602 (2022).
- [77] A. W. Sandvik, *Phys. Rev. E* **68**, 056701 (2003).
- [78] A. W. Sandvik, in *AIP Conference Proceedings*, Vol. 1297 (American Institute of Physics, 2010) pp. 135–338.
- [79] Z. Yan, Y. Wu, C. Liu, O. F. Syljuåsen, J. Lou, and Y. Chen, *Phys. Rev. B* **99**, 165135 (2019).
- [80] D. Delmastro and J. Gomis, “Symmetries of abelian chern-simons theories and arithmetic,” (2019).
- [81] M. Oshikawa, Y. B. Kim, K. Shtengel, C. Nayak, and S. Tewari, *Annals of Physics* **322**, 1477 (2007).
- [82] H. B. Xavier, C. Chamon, and R. G. Pereira, “Network construction of non-abelian chiral spin liquids,” (2022).
- [83] T. Iadecola, T. Neupert, C. Chamon, and C. Mudry, *Phys. Rev. B* **99**, 245138 (2019).
- [84] V. Bouchiat, D. Vion, P. Joyez, D. Esteve, and M. H. Devoret, *Physica Scripta* **1998**, 165 (1998).
- [85] R. G. Melko and A. W. Sandvik, *Phys. Rev. E* **72**, 026702 (2005).